

Conformal order and Poincaré-Klein mapping underlying electrostatics-driven inhomogeneity in tethered membranes

Honghui Sun and Zhenwei Yao*

*School of Physics and Astronomy, and Institute of Natural Sciences,
Shanghai Jiao Tong University, Shanghai 200240, China*

Understanding the organization of matter under the long-range electrostatic force is a fundamental problem in multiple fields. In this work, based on the electrically charged tethered membrane model, we reveal regular structures underlying the lowest-energy states of inhomogeneously stretched planar lattices by a combination of numerical simulation and analytical geometric analysis. Specifically, we show the conformal order characterized by the preserved bond angle in the lattice deformation, and reveal the Poincaré-Klein mapping underlying the electrostatics-driven inhomogeneity. The discovery of the Poincaré-Klein mapping, which connects the Poincaré disk and the Klein disk for the hyperbolic plane, implies the connection of long-range electrostatic force and hyperbolic geometry. We also discuss lattices with patterned charges of opposite signs for modulating in-plane inhomogeneity and even creating 3D shapes, which may have a connection to metamaterials design. This work suggests the geometric analysis as a promising approach for elucidating the organization of matter under the long-range force.

I. INTRODUCTION

The electrostatic force represents an important and versatile interaction to mediate the organization of materials [1, 2], especially in various self-assembly processes at the nanoscale [3, 4] and in extensive electrolyte solutions [5, 6]. For example, the electrostatic interaction has been exploited by Michael Faraday in the mid-1800s to prepare colloidal suspensions of charged gold particles that remain stable to the present day [7]. The symmetric electrostatic interaction has shown to provide the symmetry-breaking mechanism for the formation of a variety of material morphologies in multiple fields, ranging from the electrostatics-driven chirality [8, 9], the shape transitions of shells [10, 11] and ribbons [12–14], and exceedingly rich conformations of highly charged biomolecules like DNA and proteins [15–17], to the assembly of patterned surface coatings [18–20]. Through the Thomson model [21–24], where the electrically charged particles are confined on the sphere, and various generalized versions defined on planar disk [25–28] and curved surfaces [29], much has been learned about the crucial role of electrostatics in packing charged particles on confined geometries. While the confluence of theory and experiment in the past decades shows that in confined environments the electrostatic force could create unique topological defect structures and induce non-Euclidean geometries [29, 30], the question of how the electrostatic force regulates the organization of matter in free-standing charged condensed matter systems, which represent a host of entities in materials science and biology, has not yet been fully understood.

The goal of this work is to explore the electrostatic phe-

nomenon in the free-standing, electrically charged tethered membrane from the perspective of geometry, focusing on the regular structure underlying the lowest-energy particle configuration as a vestige of the convoluted relaxation process. The membrane model consists of a collection of charged particles connected by linear springs in triangular lattice. The element of elasticity is introduced to balance the repulsive electrostatic force and to hold the particles together. The elastic triangular lattice also represents the simplest organization of matter. Charged elastic membranes may be realized in surfactant bilayer systems [31, 32] and charged lamellar systems [33]. The geometry and stress of membranes under various constraints have been extensively studied [34–42]. The presence of surface charge could significantly influence the elastic rigidity [43–45] and structural stability [10, 13, 46, 47] of membranes.

In this work, we resort to the combination of numerical simulation and analytical calculation to determine and analyze the lowest-energy particle configuration, and to explore the electrostatics-based organization principle of matter. We first perform preliminary analytical analysis of the few-body 1D and 2D systems to demonstrate the complexity of the electrostatic force. The complexity arises from both the long-range nature of the electrostatic force and its interplay with the fluctuating geometry of the membrane in the relaxation process. We further identify the inhomogeneously stretched planar lattice as the lowest-energy state. Geometric analysis shows the conformal order and the preserved colinearity and concyclicity in the deformation of the membrane. Based on these key features, we reveal the Poincaré-Klein mapping underlying the electrostatics-driven inhomogeneity. The Poincaré-Klein mapping connects the Poincaré disk and the Klein disk, which represent two classical models for the hyperbolic plane. We also discuss the lowest-energy configurations of particles in lattices with patterned charges of opposite signs for modulating in-plane inhomogeneity and even creating 3D shapes, which may

*Electronic address: zyao@sjtu.edu.cn

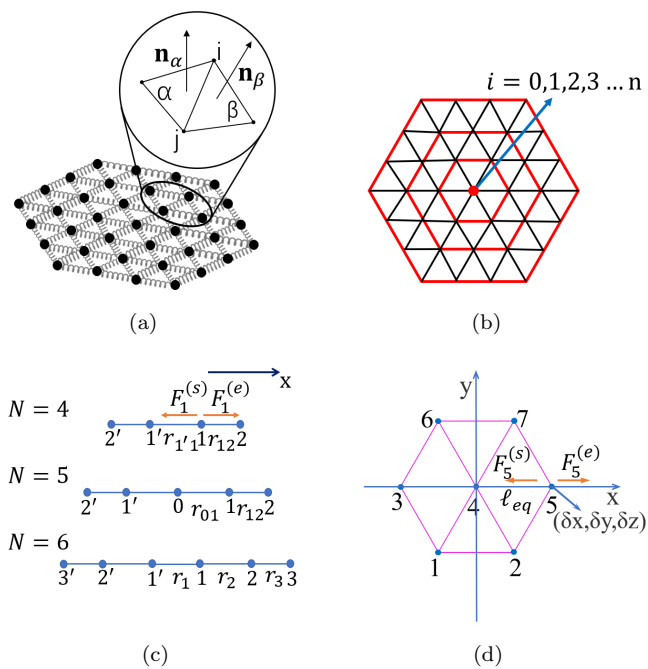


FIG. 1: Schematic plots of the model system. (a) The model consists of a collection of charged point particles connected by linear springs in triangular lattice of hexagonal shape. (b) Notation for concentric hexagonal layers. The central point is denoted as layer 0. The outermost hexagonal layer is denoted as layer n . (c) Plots of 1D systems for preliminary analysis. (d) Plot of an elementary hexagonal system ($n = 1$) for analytical analysis.

have connection to metamaterials design. These results advance our understanding on the organization of matter under the long-range force from the perspective of geometry.

II. MODEL AND METHOD

The model consists of a collection of charged point particles in triangular lattice of hexagonal shape. Each particle carries a charge of q_0 . Adjacent particles are connected by identical linear springs of stiffness k_s and balance length ℓ_0 . For convenience in discussion, the hexagonal lattice is divided into a number of layers, as shown in Fig. 1(b). The total number of particles for a triangular lattice of n layers $N = 3n^2 + 3n + 1$. For a given configuration, the total energy of the system is [48, 49]:

$$E = k_s \sum_{i \in B} (\ell_i - \ell_0)^2 + k_b \sum_{\langle \alpha, \beta \rangle} (1 - \mathbf{n}_\alpha \cdot \mathbf{n}_\beta) + k_e \sum_{i, j \in V, i \neq j} \frac{1}{r_{ij}}, \quad (1)$$

where ℓ_i is the length of the spring i , \mathbf{n}_α is the unit normal vector of the triangle α , and r_{ij} is the Euclidean distance of two particles i and j , as shown in Fig. 1(a). The three terms in Eq.(1) represent the total stretching

energy, bending energy and electrostatic energy, which are defined on the bonds, triangular faces and points in the triangular lattice, respectively. $k_e = q_0^2/4\pi\epsilon_0$, where ϵ_0 is the vacuum dielectric constant. In this work, the units of length and energy are ℓ_0 and ϵ_s , respectively, and $\epsilon_s = k_s \ell_0^2$.

We employ the standard annealing Metropolis Monte Carlo algorithm to determine the lowest-energy states of the model system under the free boundary condition [50]. The boundary particles are free of any external force except the elastic and electrostatic force from other particles as defined in Eq. (1). Given an initial configuration of tethered particles, we simultaneously move each particle by a random vector $d\hat{\omega}$, where $\hat{\omega}$ is a random unit vector in 3D space and d is the step size. The displacement vectors on the particles are statistically independent. An update of the positions of the particles is denoted as one sweep. The particle configuration is updated by consecutive sweeps until the system reaches the lowest-energy state under some specified termination conditions. Specifically, the relaxation process of the system is terminated if the standard deviation of energy in the last 5000 sweeps (denoted as δE) becomes sufficiently small. Typically, δE is as small as $10^{-2}\epsilon_s$. The value of d is in the range of $[10^{-4}\ell_0, 10^{-5}\ell_0]$. The value of the final temperature T_f in the last 5000 sweeps is in the range of $[10^{-5}\epsilon_s/k_B, 10^{-6}\epsilon_s/k_B]$, where k_B is the Boltzmann's constant.

III. RESULTS AND DISCUSSION

This section consists of two subsections. In Sec. III A, we first perform preliminary analytical analysis of the few-body 1D and 2D systems, and show the complexity of the long-range electrostatic force. By numerical simulation, we identify the inhomogeneously stretched planar lattice as the lowest-energy state in the parameter space of (k_b, k_e) across several orders of magnitude, and analyze the inhomogeneity phenomenon in terms of the bond length. We also discuss the variations of lattice shape and energy in the relaxation process. In Sec. III B, by geometric analysis, we show the conformal order and the preserved colinearity and concyclicity in the lattice deformation. Based these key geometric features, we reveal the Poincaré-Klein mapping underlying the electrostatics-driven inhomogeneity, which implies the connection of long-range electrostatic force and hyperbolic geometry. We also discuss lattices with patterned charges of opposite signs that may have a connection to metamaterials design, and briefly discuss possible realizations of the theoretical model.

A. Inhomogeneously stretched planar lattice as the lowest-energy state

We first analyze the analytically tractable 1D few-particle systems, focusing on the distribution of the particles along the line in mechanical equilibrium. The schematic plot of the N particles connected by $N - 1$ linear springs is shown in Fig. 1(c). For the case of $N = 4$, it can be shown that $r_{12} < r_{1'1}$, indicating the phenomenon of inhomogeneity under the long-range repulsive force in a 1D lattice system (see Appendix A for more information). This conclusion could be generalized to the two boundary springs in 1D systems of $N > 3$ regardless of the values of k_s and k_e . For example, for the cases of $N = 5$ and $N = 6$, based on the similar argument for the case of $N = 4$, one could derive that $r_{12} < r_{01}$ and $r_3 < r_2$, respectively. By computation, we find that a spring that is closer to the center of the 1D lattice is subject to stronger pulling force from the two groups of the particles on its two sides; it is a challenge to present a rigorous proof due to the long-range nature of the electrostatic force. In other words, the spring length decreases from the center to the ends of the 1D lattice in mechanical equilibrium.

For the 2D case, we analyze the mechanically equilibrium configuration of the elementary single-layer hexagonal system composed of only seven particles connected by linear springs, as shown in Fig. 1(d). Combination of analytical and numerical approaches confirms the stability of the flat hexagonal configuration in Fig. 1(d) (see Appendix A for more information). For a larger hexagonal system, it is expected that similar to the 1D case, the long-range repulsive force may lead to inhomogeneous distribution of particles. From the perspective of geometry, the inhomogeneity of particle distribution could be regarded as a modification of the metric structure over the lattice [36]. As such, one may inquire if a larger hexagonal lattice equipped with a spatially varying metric would be buckled to the 3D space under the electrostatic force for reducing energy.

To address this question, we employ the standard annealing Metropolis Monte Carlo algorithm to determine the lowest-energy states of larger 2D lattice systems [50]. The dimensionless quantity \tilde{h} is proposed to measure the degree of flatness of the deformed shape:

$$\tilde{h} = \frac{1}{\langle d \rangle} \sqrt{\frac{1}{N} \sum_{i=1}^N h_i^2}, \quad (2)$$

where h_i is the distance between particle i and the plane of the reference triangle spanned by the three particles located at the furthest corners of the hexagon. The average side length of the reference triangle is denoted as $\langle d \rangle$. For the cases of $n = \{1, 2, 3, 4, 5, 6, 7, 8, 9\}$, we systematically explore the parameter space of (k_b, k_e) across several orders of magnitude: $k_b = \{0.01, 0.1, 1, 10, 100\}$ and $k_e = \{0.001, 0.01, 0.1, 1, 10, 100\}$. It turns out that

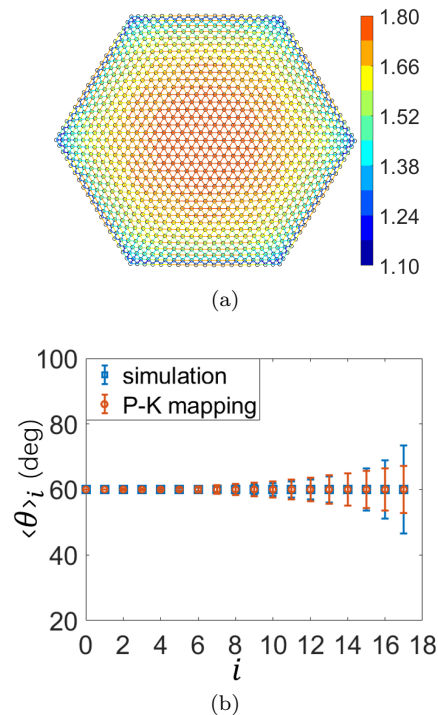


FIG. 2: Analysis of bond length and bond angle reveals conformal order in the electrostatics-driven inhomogeneity in the lowest-energy configurations. (a) The bond length gradually decreases from about 1.8 at the center to about 1.1 at the boundary, as indicated by the color legend. $n = 18$. $k_b = 0.01$. $k_e = 0.1$. (b) Distributions of the average bond angle $\langle \theta \rangle_i$ in each layer i for both the lowest-energy configuration obtained by simulations (blue square) and the configuration generated by the Poincaré-Klein mapping (orange circle). The averaging procedure in each layer is over all of the bond angles associated with each vertex along the layer [see the red hexagons in Fig. 1(b)]. The magnitude of the standard deviation is indicated by the length of the error bars. The error bars associated with simulations are slightly longer than those associated with the Poincaré-Klein mapping for $n > 14$. $n = 18$. $k_b = 0.01$. $k_e = 0.1$.

the value of \tilde{h} monotonously decreases with the reduction of temperature, and reaches a small value within the order of 10^{-3} for $T_f \sim 10^{-6} \epsilon_s / k_B$. In the relaxation process, the value of \tilde{h} shows no dependence on n . To conclude, simulations suggest that the system tends to evolve towards a stretched planar lattice as the lowest-energy state. To further substantiate this numerical observation, we also relax the lattice system on the plane (2D relaxation), and compare the energies of the fully relaxed configurations via 3D and 2D relaxations under a given low temperature, which are denoted as E_{3D} and E_{2D} , respectively. It is found that E_{2D} is always slightly smaller than E_{3D} , indicating that the energy of the fully relaxed lattice via 3D relaxation could be further lowered by flattening.

We also track the variation of the hexagonal lattice shape in the relaxation process from the per-

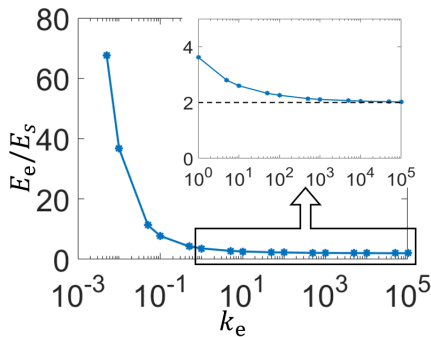


FIG. 3: Convergence of the ratio of the electrostatic energy E_e and the stretching energy E_s with the increase of k_e . $n = 6$, $k_b = 0.01$. The value of the energy is obtained for fully relaxed configuration.

spective of the integral of the Gaussian curvature for varying values of n , k_e and k_b : $n = \{1, 2, 3, 4, 5, 6, 7, 8, 9\}$, $k_b = \{0.01, 0.1, 1, 10, 100\}$ and $k_e = \{0.001, 0.01, 0.1, 1, 10, 100\}$. It turns out that the total Gaussian curvature uniformly converges to zero in all of the cases (see Appendix B for more information). We further inquire if the planar lattice as the lowest-energy state is related to the hexagonal shape. To address this question, we remove $2n_r$ rows of particles from the originally hexagon-shaped lattice, and perform simulations to determine the lowest-energy configurations. Simulations also show planar lattices as the lowest-energy states; the values of \tilde{h} of the numerically obtained lowest-energy configurations are within the order of 10^{-3} . As such, the suppression of out-of-plane deformation is not unique to the hexagonal shape of the lattice, and it shall be related to the long-range nature of the electrostatic force [27].

We further analyze the in-plane deformations in the lowest-energy planar lattices. It is found that the fully relaxed lattice in mechanical equilibrium is inhomogeneously stretched. The inhomogeneous distribution of particles is presented in Fig. 2(a). The bond length significantly decreases when approaching the boundary of the system, implying that the disruption of the lattice may be initiated from the center of the system. The degree of inhomogeneity is controlled by the characteristic length scale ℓ_{es} . Simulations at varying values of k_e (and fixed value of k_s) show that increasing ℓ_{es} leads to stronger stretching of the springs and larger variation in the distribution of the bond length over the lattice.

How shall we understand the phenomenon of inhomogeneity in the electrostatics-driven deformation of the lattice? The crucial element for shaping the inhomogeneous distribution is the combination of the long-range nature of the physical interaction and the discrepancy in the ambient environment of the particles. Specifically, in the hexagonal lattice, each particle “sees” distinct distributions of the other particles (except the particles located at the lattice sites of C_6 symmetry), ultimately leading to spatially varying electrostatic force over the lattice in mechanical equilibrium. Simulations show that the

deformation towards the center of the hexagonal lattice in mechanical equilibrium is larger for compensating the stronger electrostatic repulsion.

Regarding the energetics in the relaxation process, the variation of the ratio of the electrostatic energy E_e to the stretching energy E_s for the stretched lattices in mechanical equilibrium is plotted in Fig. 3; the bending energy is vanishingly small. With the stretching of the lattice, the ratio E_e/E_s decreases, indicating the conversion of the electrostatic energy to the stretching energy. With the increase of k_e up to 10^5 , the ratio E_e/E_s converges to about 2; statistics of the cases of varying n from 1 to 9 shows that $E_e/E_s = 2.030 \pm 0.003$ for $k_e = 10^5$.

To understand the convergence of the ratio E_e/E_s to the common limiting value of about 2, we present the analytical result for the two-particle system. From the balance of the electrostatic force and the elastic stretching force, we solve for the equilibrium configuration of the system and calculate the limiting value of the energy ratio:

$$\lim_{k_e \rightarrow \infty} \frac{E_e}{E_s} = \lim_{k_e \rightarrow \infty} \frac{2\ell_{es}^3}{\ell_{eq}(\ell_{eq} - \ell_0)^2} = 2, \quad (3)$$

where the equilibrium distance ℓ_{eq} of the two particles could be derived from the force balance equation and $\ell_{es} = (k_e/k_s)^{1/3}$. The characteristic length scale ℓ_{es} arises from the competition of the electrostatic force and the elastic force. The expression for ℓ_{eq} has the same form as Eq.(12) by replacing $\tilde{\gamma}$ for $\ell_{es}^3/(2\ell_0^3)$. In the limit of $k_e \rightarrow \infty$, $\ell_{eq} \sim k_e^{1/3}$. The analytical result for the two-particle system and the numerical results for the large systems suggest that the partition of the electrostatic energy and the elastic stretching energy conforms to a constant ratio of 2 in the limit of large k_e .

B. Conformal order and Poincaré-Klein mapping underlying the stretched planar lattice

In the preceding subsection, we have revealed the inhomogeneously stretched planar lattice as the lowest-energy configuration under the competing electrostatic force and elastic force. In this subsection, we focus on analyzing the geometric structures underlying the inhomogeneity phenomenon.

To seek the regularity underlying the inhomogeneous particle distribution, we analyze the distribution of the bond angle, and inquire if the bond angle is invariant in the electrostatics-driven deformation of the lattice. In mathematics, strictly angle-preserved deformation is known as conformal transformation. Quasi-conformal order has been revealed in the beautiful gravity’s rainbow formed by electrically charged steel beads in gravity field [51–53]. Recently, quasi-conformal order has been reported in the inhomogeneous packings of long-range repulsive particles confined on the disk [28], self-assembled vortices in a type-II superconducting disk [54] and Lennard-Jones particles confined on the sphere [55].

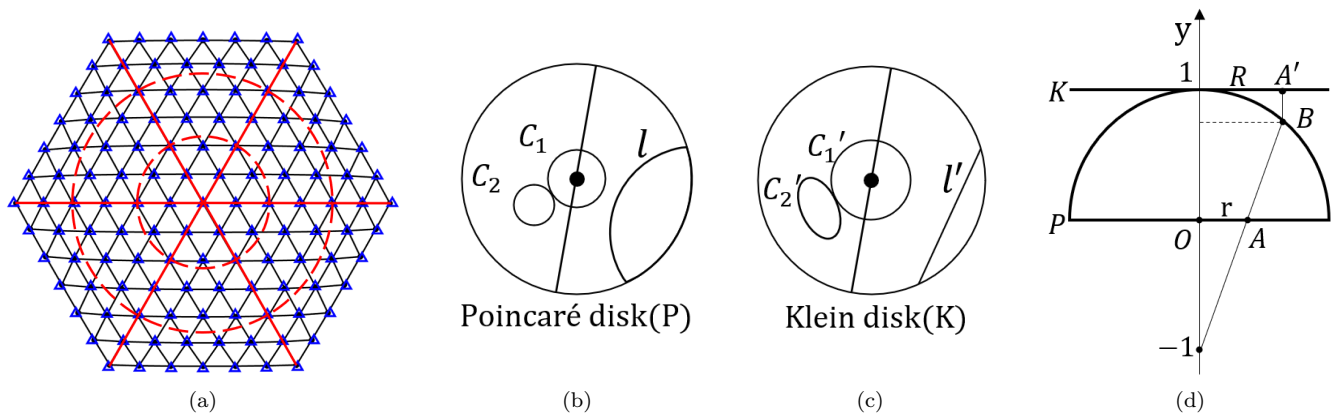


FIG. 4: Poincaré-Klein mapping underlying the electrostatics-driven inhomogeneity in the lowest-energy configurations. (a) The configuration obtained by simulations (solid black dots) is well fitted by the theoretical configuration generated by Poincaré-Klein mapping (empty blue triangles). The values of the fitting parameters in Eq.(7) are: $\lambda = 0.032$, $\Gamma = 22.028$. $L = 0.005$. $n = 6$. $k_b = 0.01$. $k_e = 0.1$. An infinitely large hyperbolic disk is represented in the Poincaré disk (b) and Klein disk (c). l and l' correspond to hyperbolic geodesics in these two models. Circles on the hyperbolic plane preserve their shape in the Poincaré disk [C_1 and C_2 in Fig. 4(b)]. In contrast, only concentric circles preserve their shape in the Klein disk [C'_1 and C'_2 in Fig. 4(c)]. Quantitative information about the two models is presented in the paper. (d) Illustration of the Poincaré-Klein mapping. The Poincaré disk and the Klein disk are indicated by the two lines labeled as P and K, respectively. The semicircle between represents a semi-sphere. Any point in the Poincaré disk (labeled as A) is mapped to A' in the Klein disk. The line BA' is perpendicular to the disk K.

The plot of the bond angle along the layers of the lattice is shown in Fig. 2(b). A key observation is that the average bond angle is uniformly 60 degrees; the standard deviation increases when approaching the boundary. Therefore, the deformation of the interior region of the lattice could be regarded as conformal. In other words, each triangular cell in the interior region experiences isotropic expansion according to the geometric property of conformal transformation [51]. Furthermore, in the sense of average bond angle, the lattice deformation is quasi-conformal. We also vary the values of n and k_e (see Appendix B). It is found that the average bond angle is uniformly 60 degrees as the value of k_e is varied by several orders of magnitude, indicating that the preserved average bond angle is a common feature in the electrostatics-driven deformation of the lattice. Note that in the measurement of bond angles in the deformed lattice, the vertices are connected by straight lines. However, the lattice is bent in the continuum limit. Using smooth curves instead of straight lines to connect vertices may reduce the magnitude of the error bar especially near the boundary in Fig. 2(b) [51].

In addition to the invariant bond angle, are there any other invariant properties in the deformation of the lattice? Scrutiny of the lowest-energy configurations reveals some common features that are illustrated in Fig. 4(a). First, the particles remain on the principal axes (the three solid red lines) of the triangular latticed in the deformation. Second, the particles remain on the concentric circles (the dashed red circle) in the deformation. For the case in Fig. 4(a), the mean deviations of the points both from the three principal axes and from the concentric cir-

cles are at the order of 10^{-2} . Third, the bond length is appreciably shorter when approaching the boundary of the system. These geometric features inspire us to explore the mathematical structure underlying the deformation. Specifically, we search for a mapping that could reproduce these key features in the in-plane deformation.

The Poincaré disk and the Klein disk represent two kinds of important models for representing the infinitely large 2D hyperbolic plane in an open unit disk in 2D Euclidean space [56]. Notably, the concept of hyperbolic geometry is widely applied to the analysis of complex networks in recent years [57, 58]. Hyperbolic geodesics are mapped to arcs in the Poincaré disk, and to straight lines in the Klein disk, as indicated by l and l' in Fig. 4(b) and Fig. 4(c). Circles on the hyperbolic plane preserve their shape in the Poincaré disk [C_1 and C_2 in Fig. 4(b)]. In contrast, only concentric circles preserve their shape in the Klein disk [C'_1 and C'_2 in Fig. 4(c)]. These features could be rigorously derived from the metric tensor over the disk. The line element ds in the Poincaré disk is [56]

$$ds^2 = \frac{4\|\mathbf{dx}\|^2}{(1 - \|\mathbf{x}\|^2)^2}, \quad (4)$$

where $\mathbf{x} = (x_1, x_2)$, and $\|\cdot\|$ denotes the Euclidean norm. $\|\mathbf{x}\| \leq 1$. The line element ds in the Klein disk is [56]

$$ds^2 = \frac{\|\mathbf{dx}\|^2}{1 - \|\mathbf{x}\|^2} + \frac{(\mathbf{x} \cdot \mathbf{dx})^2}{(1 - \|\mathbf{x}\|^2)^2}, \quad (5)$$

where $\|\mathbf{x}\| \leq 1$.

These two kinds of models are connected by the Poincaré-Klein mapping [56] (see Appendix D for more

information):

$$f(z) = \frac{2z}{1 + |z|^2}, \quad |z| \leq 1 \quad (6)$$

Equation (6) states that a point A at z in the Poincaré disk is mapped to the point A' at $f(z)$ in the Klein disk. The Poincaré-Klein mapping in Eq. (6) is illustrated in Fig. 4(d). The semicircle between the lines K and P represents a hemisphere of unit radius. The Poincaré disk and the Klein disk are represented by the lines P and K, respectively.

In order to characterize the deformation of the lattice, we rescale Eq.(6) by introducing two parameters λ and Γ :

$$w(z; \lambda, \Gamma) = \Gamma \frac{2\lambda z}{1 + \lambda^2 |z|^2}. \quad (7)$$

The generalized Poincaré-Klein mapping in Eq. (7) preserves the key features in the deformation of the lattice. First, two arbitrary points on a radial line in the z plane denoted as $z_1 = r_1 e^{i\theta}$ and $z_2 = r_2 e^{i\theta}$ are mapped to $w_1 = \alpha_1 e^{i\theta}$ and $w_2 = \alpha_2 e^{i\theta}$, where $\alpha_i = \Gamma \frac{2\lambda r_i}{1 + \lambda^2 r_i^2}$. The new points are still on the same radial line. Second, two arbitrary points on a concentric circle denoted as $z_1 = r e^{i\theta_1}$ and $z_2 = r e^{i\theta_2}$ are mapped to $w_1 = \beta e^{i\theta_1}$ and $w_2 = \beta e^{i\theta_2}$, where $\beta = \Gamma \frac{2\lambda r}{1 + \lambda^2 r^2}$. The new points remain on a concentric circle.

Now, we search for the optimal values of the parameters λ and Γ in Eq.(7) for fitting the deformation of the lattice. Specifically, the optimal values of λ and Γ are determined by minimizing the deviation of the configuration generated by the Poincaré-Klein mapping from the lowest-energy configuration obtained in simulations. The dimensionless quantity to be minimized is: $L = \langle \delta r \rangle / \langle \ell \rangle$.

$\langle \delta r \rangle = \sqrt{\sum_{i=1}^N [(x_i^s - x_i^m)^2 + (y_i^s - y_i^m)^2]} / N$, where the superscripts of s and m indicate the data from the simulation and the Poincaré-Klein mapping. $\langle \ell \rangle$ is the average bond length in the lowest-energy configurations. We work in the discretized parameter space of λ and Γ . $\lambda \in (0, 1)$ and $\Gamma \in (0, 100)$ in the resolution of $\delta\lambda = \delta\Gamma = 10^{-3}$.

Figure 4(a) shows that the configuration generated by the Poincaré-Klein mapping (marked as empty blue triangles) agrees well with the deformed lattice in mechanical equilibrium (solid black dots connected by bonds) for the case of $n = 6$. We also check larger systems up to $n = 18$ and a series of values of k_e ranging from 0.001 to 100, and find good agreement of the configurations generated by the Poincaré-Klein mapping and those by simulations. For example, for $k_e = 100$, the values of L (an indicator for the deviation of the lattices generated by simulations and by the Poincaré-Klein mapping) for both cases of $n = 6$ and $n = 18$ are approximately equal to 0.006; the lattices are strongly stretched for $k_e = 100$.

Furthermore, we check nonhexagonal cases. For the circular and the triangular lattices as shown in Fig. 5, simulations show that the lowest-energy configurations of

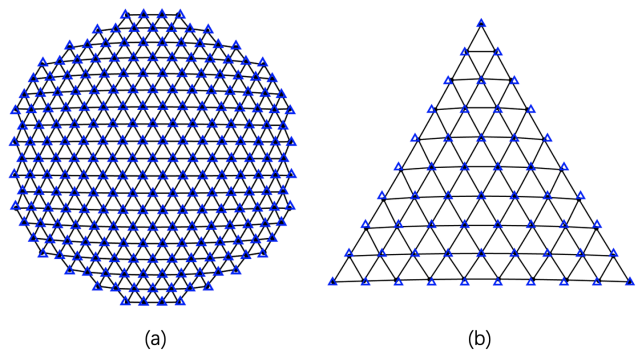


FIG. 5: Presence of Poincaré-Klein mapping in nonhexagonal lowest-energy lattices. The lowest-energy configurations of the circular (a) and triangular (b) lattices obtained by simulations (solid black dots) are well fitted by the theoretical configurations generated by Poincaré-Klein mapping (empty blue triangles). The values of the fitting parameters in Eq.(7) are: (a) $\lambda = 0.04$, $\Gamma = 19.20$. $L \approx 0.003$. (b) $\lambda = 0.01$, $\Gamma = 63.88$. $L \approx 0.010$. In both cases, $k_b = 0.01$, $k_e = 0.1$.

both cases are still well fitted by the Poincaré-Klein mapping. Note that due to the discreteness of the crystalline lattice, the circular lattice in Fig. 5(a) possesses the C_6 symmetry. Recall that the existence of the Poincaré-Klein mapping relies on the preserved colinearity and concyclicity in lattice deformation. Therefore, it is expected that the Poincaré-Klein mapping structure exists in lattices of certain symmetries for which the key features of colinearity and concyclicity are preserved in the deformation. To study the deviation of the deformations with respect to the Poincaré-Klein mapping, we also check truncated hexagonal shapes. Such anisotropic shapes are created by removing n_r rows of particles from two opposite edges in the hexagon-shaped lattice (see Appendix B for the shapes of truncated hexagonal membranes). In the cases of $n_r = \{0, 2, 4, 8\}$ for $n = 9$, $k_b = 0.01$ and $k_e = 1$, we analyze the deviation of the lowest-energy lattices generated by simulations and by the Poincaré-Klein mapping, which is characterized by L . It is found that the value of L monotonously increases from 0.004, 0.017, 0.031 to 0.042 as the value of n_r is increased from 0, 2, 4 to 8, respectively. In other words, the deviation of the deformation with respect to the Poincaré-Klein mapping is enlarged with the enhanced anisotropy of the lattice shape.

In Fig. 2(b), we also show the distribution of the bond angle in each layer of the lattice for the configuration generated by the Poincaré-Klein mapping. While the deformation in the central region of the lattice could be regarded as conformal, the lattice deformation as a whole is quasiconformal in the sense of average bond angle. In fact, the condition for the formation of strictly conformal lattice is critical; no uniform field could stabilize a perfect conformal crystal with the inverse power potential [53]. Strictly speaking, for the deformation defined by Eq.(7), only the deformation at the origin is conformal for the

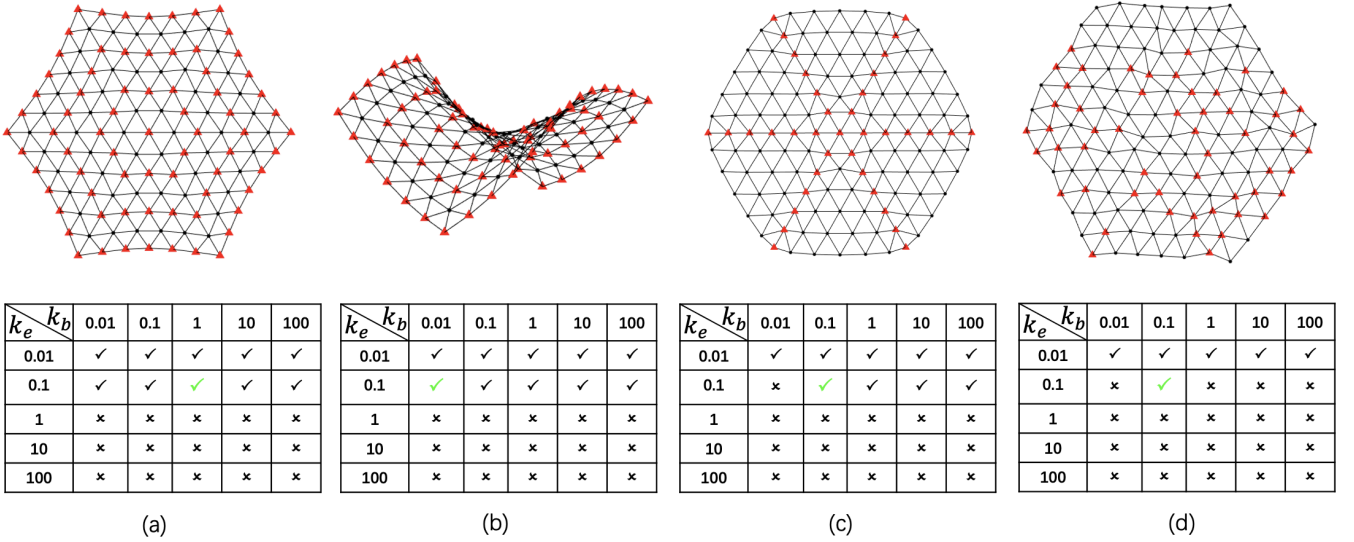


FIG. 6: Lowest-energy states of the lattices under typical distributions of charges. The red triangles represent particles carrying charges of the same sign; the remaining particles are oppositely charged. The cases that charges of opposite signs stick together are marked by the cross symbols in the tables for the corresponding charge distributions; nonstick cases are marked by the tick symbols. The values of k_e and k_b for the lattice shapes are in green in the tables. $\{k_e, k_b\} = \{0.1, 1\}$ (a), $\{0.1, 0.01\}$ (b), $\{0.1, 0.1\}$ (c) and $\{0.1, 0.1\}$ (d). $k_s = 1$.

following reason.

According to the geometric property of conformal transformation, no shearing occurs in the deformation for preserving the angle. For the deformation characterized by $g(z) = u(x, y) + iv(x, y)$ ($z = x + iy$), the strain field could be derived as [52]

$$\begin{aligned}
 u_{xx} &= \frac{1}{2} \left[\left(\frac{\partial u}{\partial x} \right)^2 + \left(\frac{\partial v}{\partial x} \right)^2 - 1 \right], \\
 u_{yy} &= \frac{1}{2} \left[\left(\frac{\partial u}{\partial y} \right)^2 + \left(\frac{\partial v}{\partial y} \right)^2 - 1 \right], \\
 u_{xy} &= u_{yx} = \frac{1}{2} \left(\frac{\partial u}{\partial x} \frac{\partial u}{\partial y} + \frac{\partial v}{\partial x} \frac{\partial v}{\partial y} \right).
 \end{aligned} \tag{8}$$

Note that a typo in Ref. [52] has been corrected in Eqs.(8). It is straightforward to check that $u_{xy} = u_{yx} = 0$ and $u_{xx} = u_{yy}$ if $g(z)$ satisfies the Cauchy-Riemann conditions [59]:

$$\frac{\partial u}{\partial x} = \frac{\partial v}{\partial y}, \quad \frac{\partial u}{\partial y} = -\frac{\partial v}{\partial x}. \tag{9}$$

For $w(z; \lambda, \Gamma)$ in Eq.(7), the Cauchy-Riemann conditions are satisfied only at $z = 0$. As such, the deformation as characterized by Eq.(7) is strictly conformal only at the origin of the system. The $z = 0$ point in the continuum description of Eq.(7) corresponds to an area containing a number of particles in the discretized particle system.

Here, we emphasize that the revealed Poincaré-Klein mapping underlying the electrostatics-driven inhomogeneity in tethered membranes is based on the invariant properties in the large deformation of the lattice. Note

that, considering the complexity of the long-range interaction in organizing particles, it is important to focus on the invariant elements in the deformation. Specifically, the key features of the preserved colinearity and concyclicity in the strongly deformed lattice provide important clues for uncovering the connection with hyperbolic geometry. In comparison with the classical scenario of a stretched elastic disk by applying force on the boundary, which results in homogeneous strain field [60] (see Appendix C for more information), the electrostatic force creates inhomogeneity in the hexagon-shaped lattice system, which in turn encodes the information of how electrostatics regulates the distribution of matter. As such, geometric analysis of the inhomogeneity phenomenon represents an important approach for extracting such information. For example, in the context of this work, the unique geometric perspective of the Poincaré-Klein mapping is useful for capturing the characteristic invariant features of colinearity and concyclicity in the lattice deformation as well as suggesting the connection of long-range force and hyperbolic geometry.

We also discuss the extension of the current study by tailoring the distributions of charges of different signs for targeted shapes with potential connection to metamaterials design, as inspired by the suggestion of the anonymous referee. The lowest-energy states of the lattices under typical distributions of charges are presented in Fig. 6, where the red triangles represent particles carrying charges of the same sign; the remaining particles are oppositely charged. In Figs. 6(a) and 6(b), the red triangles are along concentric hexagons. In Figs. 6(c) and 6(d), the red triangles are along the three principal axes and are randomly distributed, respectively. These

systems are relaxed by the annealing Metropolis Monte Carlo algorithm. The expression for the total energy of the system is the same as Eq. (1) except the last term whose sign becomes negative if the pair of points i and j carry opposite charges. Systematic study of the lattice system at varying values of k_e and k_b shows that charges of opposite signs stick together for large k_e . Such cases are indicated by the cross symbols in the tables for the corresponding charge distributions in Fig. 6; nonstick cases are marked by the tick symbols. The values of k_e and k_b for the presented lattice shapes are in green in the tables.

From Figs. 6(a) and 6(b), we see that the originally quasiplanar lattice becomes a saddle-like shape as the bending rigidity is reduced from $k_b = 1$ to $k_b = 0.01$; the amount of the out-of-plane deformation in the lattice in Fig. 6(a) is at the order of 10^{-2} . The saddle-like shape becomes more curved with the reduction of the value of k_b from 0.1 to 0.01. The formation of the negatively curved saddle-like shape could be attributed to the circumferential expansion and the radial shrinking of the lattice under the electrostatic force [56]. The lowest-energy shapes of the lattices in Figs. 6(c) and 6(d) are quasiplanar. The amount of the out-of-plane deformations is at the order of 10^{-2} . These results demonstrate the modulation of both the lattice shape and the in-plane particle arrangement by the design of charge pattern.

We finally briefly discuss possible experimental realizations of the theoretical model. One may employ charged beads to fabricate the experimental system as introduced in a recent work on the experimental realization of the theoretical model of charged beads on a string in polymer science [61]. In Ref. [61], the system comprises electrically charged, millimeter-scale Teflon and Nylon beads placed on a paper over a flat aluminum sheet. To fabricate a tethered membrane corresponding to our theoretical model, one may employ these electrically charged beads and introduce elastic springs. In addition to the above-mentioned macroscopic beads system, one may also resort to electrically charged colloids confined on liquid interface for constructing a flat tethered membrane. The effective interactions between colloids are tunable. To obtain the approximately Coulombic interaction, the Debye length in the Yukawa interaction could be increased by reducing the salt concentration [3, 62] and minimizing the image-charge effect [63].

IV. CONCLUSION

In summary, the theme of this work is to analyze the deformations of tethered membranes under the combined electrostatic and elastic forces. The triangular lattice system provides a suitable model for understanding the organization of matter by the long-range electrostatic force. The long-range nature of the electrostatic force and its complicated interplay with the fluctuating geometry of the membrane impose a challenge to this prob-

lem. By combination of numerical simulation and analytical geometric analysis, we show the crucial role of the long-range electrostatic force for the suppression of out-of-plane deformations and the formation of inhomogeneity in the lowest-energy configurations. Especially, we highlight the revealed Poincaré-Klein mapping that captures the invariant geometric features in the inhomogeneous deformation and also implies the connection of long-range repulsive force and hyperbolic geometry. This work suggests the geometric analysis as a promising approach for elucidating the inhomogeneous organization of matter under the long-range force. As inspired by the suggestion of the anonymous referee, it is of interest to extend the current study by tailoring the charge patterns of different signs for targeted shapes and particle distributions, which may have connection to metamaterials design. Preliminary results demonstrate the modulation of in-plane inhomogeneity and the appearance of saddle-like shapes under different kinds of charge patterns.

Appendix A: Preliminary analytical analysis of 1D & 2D systems

The schematic plot of 1D system consisting of N particles connected by $N - 1$ linear springs is shown in Fig. 1(c). For the trivial case of $N = 3$, the lengths of the two springs are identical. For the case of $N = 4$, $r_{12} < r_{1'1}$. A proof by *reductio ad absurdum* is presented below. Suppose $r_{12} \geq r_{1'1}$, the total elastic force on particle 1, $\vec{F}_1^{(s)} = k_s(r_{12} - r_{1'1})\hat{x}$, is either pointing rightward or zero. Consequently, the total electrostatic force $\vec{F}_1^{(e)}$ on particle 1 is either pointing leftward or zero to satisfy the force balance condition. However, the supposed condition of $r_{12} \geq r_{1'1}$ leads to an electrostatic force on particle 1 pointing rightward. This contradiction indicates the impossibility of $r_{12} \geq r_{1'1}$. Therefore, for the case of $N = 4$, r_{12} is always smaller than $r_{1'1}$.

For the 2D case, we perform analysis of the mechanically equilibrium configuration of the elementary single-layer hexagonal system composed of only seven particles connected by linear springs, as shown in Fig. 1(d). The hexagonal configuration is confined on the plane. For an arbitrary particle on the boundary denoted as 5 in Fig. 1(d), the balance of the electrostatic force $F_5^{(e)}$ and the elastic stretching force $F_5^{(s)}$ along the x axis leads to

$$2k_s(\ell_{eq} - \ell_0) = \frac{k_e}{\ell_{eq}^2} \left(\frac{\sqrt{3}}{3} + \frac{9}{4} \right), \quad (10)$$

where ℓ_{eq} is the equilibrium bond length, and

$$\ell_{es} = \left(\frac{k_e}{k_s} \right)^{\frac{1}{3}}. \quad (11)$$

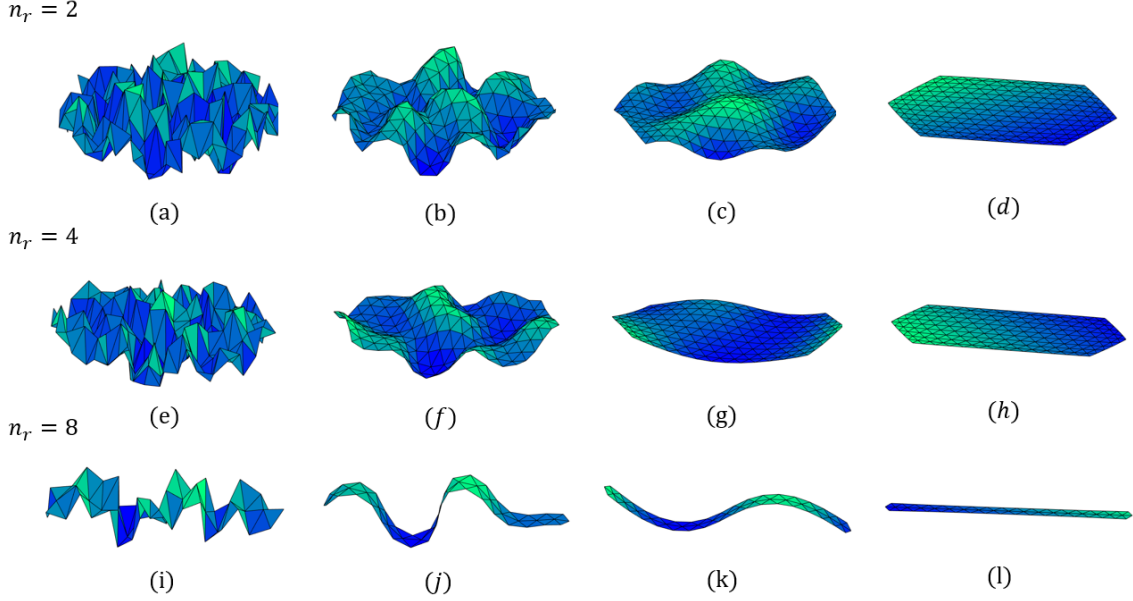


FIG. 7: Relaxations of truncated hexagonal membranes under the electrostatic force. n_r rows of particles are removed from two opposite edges in the hexagon-shaped lattice. Typical membrane shapes in the relaxation process are presented for each case. For visual convenience, the color of the figures is rendered by the heights of the triangles in the lattice; the brighter triangles are located at a larger height. In the lowest-energy shapes, $\tilde{h} = 8.02 \times 10^{-5}$ (d), 9.78×10^{-5} (h), and 2.53×10^{-4} (l), respectively. $n = 9$, $k_b = 0.01$, $k_e = 100$.

From Eq. (10), we obtain

$$\frac{\ell_{eq}}{\ell_0} = \left(\tilde{\gamma} + \frac{1}{27} + \sqrt{\left(\tilde{\gamma} + \frac{1}{27}\right)^2 - \left(\frac{1}{27}\right)^2} \right)^{\frac{1}{3}} + \left(\tilde{\gamma} + \frac{1}{27} - \sqrt{\left(\tilde{\gamma} + \frac{1}{27}\right)^2 - \left(\frac{1}{27}\right)^2} \right)^{\frac{1}{3}} + \frac{1}{3}, \quad (12)$$

where

$$\tilde{\gamma} = \left(\frac{\sqrt{3}}{12} + \frac{9}{16} \right) \frac{\ell_{es}^3}{\ell_0^3}. \quad (13)$$

The dimensionless quantity $\tilde{\gamma}$ reflects the competition of the electrostatic force and the elastic force.

It is of interest to discuss Eq.(12) in the limiting cases of $\tilde{\gamma} \rightarrow 0$ (strong spring stiffness) and $\tilde{\gamma} \rightarrow \infty$ (strong electrostatic effect). As $\tilde{\gamma} \rightarrow 0$,

$$\frac{\ell_{eq}}{\ell_0} = 1 + 2\tilde{\gamma} - 8\tilde{\gamma}^2 + o(\tilde{\gamma}^2). \quad (14)$$

It is reasonable that $\ell_{eq} = \ell_0$ when $\tilde{\gamma} = 0$ (i.e., $k_e = 0$). In contrast, the asymptotic expression for ℓ_{eq} as $\tilde{\gamma} \rightarrow \infty$ is

$$\frac{\ell_{eq}}{\ell_0} = (2\tilde{\gamma})^{\frac{1}{3}} = \beta \frac{\ell_{es}}{\ell_0}, \quad (15)$$

where $\beta = \left(\frac{\sqrt{3}}{6} + \frac{9}{8} \right)^{\frac{1}{3}} \approx 1.12$. The exponent 1/3 in Eq. (15) originates from the cubic term in Eq. (10), which

arises from the competition of the elastic force and the electrostatic force.

Previous study shows the counterintuitive instability of charged elastic rings under the long-range electrostatic force [64]. Here, it is of interest to examine the possible out-of-plane deformation of the elementary hexagonal configuration in Fig. 1(d). To this end, we first impose a random perturbation $\delta\vec{r}$ in 3D space on an arbitrary particle labeled 5, and calculate the variation of energy. $\delta\vec{r} = (\delta x, \delta y, \delta z)$. The resulting variation of the total energy is

$$\delta E = k_e \sum_{i=1, i \neq 5}^7 \left(\frac{1}{|\vec{r}_{i5} + \delta\vec{r}|} - \frac{1}{|\vec{r}_{i5}|} \right) + \frac{k_s}{2} \sum_{i=2,4,7} [(|\vec{r}_{i5} + \delta\vec{r}| - \ell_0)^2 - (|\vec{r}_{i5}| - \ell_0)^2], \quad (16)$$

where $|\vec{r}_{i5}|$ is the distance between particle i and 5. Keeping up to the second order terms, Eq.(16) becomes

$$\delta E = C_{11}\delta x^2 + C_{22}\delta y^2 + C_{33}\delta z^2, \quad (17)$$

where

$$\begin{aligned} \frac{C_{11}}{k_s} &= \frac{\ell_{es}^3}{4\ell_{eq}^3} \left(\frac{19\sqrt{3}}{18} + \frac{55}{8} \right) + \frac{3}{4}, \\ \frac{C_{22}}{k_s} &= \frac{\ell_{es}^3}{4\ell_{eq}^3} \left(\frac{7\sqrt{3}}{18} + \frac{49}{8} \right) + \frac{3}{4}, \\ \frac{C_{33}}{k_s} &= \frac{\ell_{es}^3}{4\ell_{eq}^3} \left(\frac{5\sqrt{3}}{9} + \frac{1}{2} \right). \end{aligned} \quad (18)$$

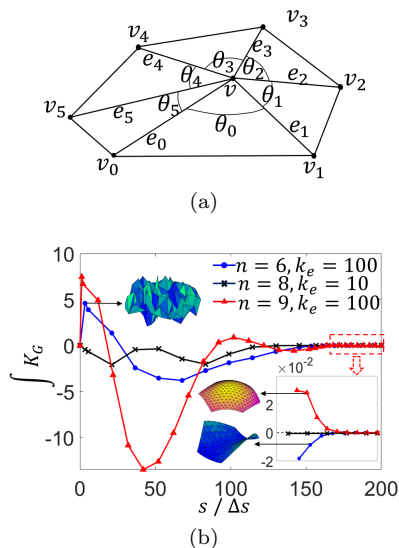


FIG. 8: Analysis of the relaxation process of the 2D system from the perspective of the variation of the Gaussian curvature. (a) Notations for the calculation of the Gaussian curvature in the main text. (b) Variation of the total Gaussian curvature over the whole lattice in the relaxation process. s represents the number of simulation steps. $\Delta s = 9000, 9000, 25000$ for the curves of $n = 6$, $n = 8$ and $n = 9$, respectively. $k_b = 0.01$. The zoomed-in inset shows the convergence of the integrated Gaussian curvature to zero.

All of these coefficients are positive. Therefore, $\delta E > 0$. In other words, the system is stable under arbitrary perturbation of any particle.

We further examine the case where all of the particles in Fig. 1(d) are perturbed by performing numerical simulations. The magnitude of the statistically independent random perturbation on each particle is restricted within the range from $-0.3\ell_{eq}$ to $0.3\ell_{eq}$. For each given value of k_e in $\{0.001, 0.01, 0.1, 1, 10, 100\}$, we generate 10^4 statistically independent particle configurations, and compute the variation of energy by Eq. (16). It turns out that the energy is always increased upon simultaneous perturbation on every particle.

To conclude, the stability of the flat hexagonal configuration in Fig. 1(d) is confirmed by combination of analytical and numerical approaches.

Appendix B: More information about the relaxation process and the bond-angle distributions in fully relaxed lattices

In this appendix, we present more information about the relaxation of truncated hexagonal membranes and the variation of the lattice shape in the relaxation process. We also present the distributions of the bond angle along the layers of the lattice in the fully relaxed lattices at varying k_e .

In the main text, the stretched planar shape has been

identified as the lowest-energy state of the hexagonal membrane under the long-range electrostatic force. To check if the flatness of the membrane is related to the hexagonal shape, we further discuss the relaxation of truncated hexagonal membranes. Specifically, we remove n_r rows of particles from two opposite edges in the hexagonal-shaped lattice, and obtain truncated hexagonal lattices with broken C_6 symmetry as shown in Fig. 7. These elongated lattices are fully relaxed by the same procedure as in the main text.

We systematically check truncated hexagonal membranes of varying size in the broad parameter space of k_e and k_b : $k_e = \{0.001, 0.01, 0.1, 1, 10, 100\}$, and $k_b = \{0.01, 0.1, 1, 10, 100\}$. $n = \{2, 3, 4, 5, 6, 7, 8, 9\}$. For each given value of n , $n_r = \{1, \dots, n-1\}$. It turns out that the truncated membranes uniformly converge to the flat shape in all of the cases. Some typical cases are shown in Fig. 7. The value of the dimensionless quantity \tilde{h} , which is introduced to characterize the degree of the out-of-plane deformation in the main text, is within the order of 10^{-3} in all of the cases in our simulations. To conclude, this observation clearly shows that the flat lowest-energy shapes are uncorrelated to the hexagonal shape of the membrane.

Furthermore, we track the variation of the hexagonal lattice shape in the relaxation process from the perspective of the integral of the Gaussian curvature. For a smooth surface Ω with piecewise smooth boundary consisting of p regular curves denoted as $C_1 \dots C_p$, according to the generalized Gauss-Bonnet theorem [65], the integral of the Gaussian curvature is:

$$\int_{\Omega} K_G dA = 2\pi\chi(\Omega) - \sum_{i=1}^p \int_{C_i} k_g ds - \sum_{i=1}^p \gamma_i, \quad (19)$$

where $\chi(\Omega)$ is the Euler characteristic of the surface Ω . k_g is the geodesic curvature. γ_i is the turning angle from curve C_i to C_{i+1} at their meeting point; $C_{p+1} = C_1$.

Note that within our numerical precision the following expression is verified to be an invariant in the relaxation of the lattice:

$$\int_{\Omega} K_G dA + \sum_{i=1}^p \gamma_i. \quad (20)$$

The temporally varying values of the first and the second terms for the case of $n = 6$ are presented in Table I. It is found that the value of the expression in Eq. (20) is very close to 2π ; $2\pi \approx 6.2831853$. In comparison with Eq. (19), the integral of the geodesic curvature is vanishingly small in the entire relaxation process of the lattice. As such, Eq. (19) is verified within our numerical precision.

Now we apply Eq.(19) to our triangular lattice system, and obtain the expression for the integral of the Gaussian curvature over the hexagonal cell (denoted as S_v)

Number of steps ($\times 10^4$)	0	3	5	19	61	89	117	138	180
$\int_{\Omega} K_G dA$	0	4.589743	3.885128	1.352282	-3.802723	-1.881432	-0.658368	-0.078556	0.000004
$\sum_i \gamma_i$	6.283185	1.693442	2.398058	4.930903	10.085908	8.164617	6.941553	6.361742	6.283181
$\int_{\Omega} K_G dA + \sum_i \gamma_i$	6.283185	6.283185	6.283186	6.283185	6.283185	6.283185	6.283185	6.283186	6.283185

TABLE I: Variations of the integral of the Gaussian curvature ($\int_{\Omega} K_G dA$) and the sum of the turning angles ($\sum_i \gamma_i$) in the relaxation of the lattice. The numbers in the bottom line are very close to 2π ; $2\pi \approx 6.2831853$. The generalized Gauss-Bonnet theorem is thus verified within our numerical precision. $n = 6$. $k_b = 0.01$. $k_e = 100$.

surrounding the vertex v as shown in Fig. 8(a):

$$\int_{S_v} K_G dA = 2\pi - \sum_{i=0}^k \theta_i, \quad (21)$$

where θ_i is the angle of the two adjacent bonds vv_i and vv_{i+1} . Note that $\chi(S_v) = 1$, and $\sum_i \gamma_i = \sum_i \theta_i$. In the derivation for Eq.(21), it is assumed that the boundary curve is geodesic. By the sum of the integrated Gaussian curvature in Eq.(21) over the whole lattice, we obtain the total Gaussian curvature.

We systematically track the variation of the total Gaussian curvature in the relaxation process for varying values of n , k_e and k_b : $n = \{1, 2, 3, 4, 5, 6, 7, 8, 9\}$, $k_b = \{0.01, 0.1, 1, 10, 100\}$ and $k_e = \{0.001, 0.01, 0.1, 1, 10, 100\}$. The main results are summarized in Fig. 8(b). We see that the total Gaussian curvature uniformly converges to zero in all of the cases. Oscillation of the curve occurs in the relaxation process, indicating the exploration of the system into both positively and negatively curved shapes (see the inset figure). Closer examination of 54 oscillating curves shows the preference of negatively curved shapes (46 out of 54) in the final stage of the relaxation process. This observation implies that thermal fluctuation tends to deform the membrane to the hyperbolic shape. The inset figures also show the smoothening of the shape with the reduction of temperature.

In Fig. 9, the distributions of the bond angle along the layers of the lattice in the lowest-energy states at varying k_e are presented. We see that the average bond angle is uniformly 60 degrees as the value of k_e is varied from $k_e = 0.01$ (a), $k_e = 1$ (b), and $k_e = 100$ (c). It indicates that the preserved average bond angle is a common feature in the electrostatics-driven deformation of the lattice. In the central region of the lattice, the bond angle is well preserved in the deformation. We also notice that the magnitude of the standard deviation in the bond-angle distribution increases as the value of k_e is increased.

Appendix C: Elasticity analysis of elastic disk upon stretching

In this appendix, we present analytical continuum elasticity analysis of an isotropic elastic disk by applying a radial outward force on the boundary.

The distribution of stress over the disk in mechanical equilibrium is governed by the following equation of equilibrium [60]:

$$\partial_k \sigma_{ik} = 0, \quad i, k = x, y. \quad (22)$$

In the following, we rewrite Eq.(22) in terms of the displacement vector $\mathbf{u}(\mathbf{x})$.

The stress-strain relation is given by

$$\begin{cases} \sigma_{xx} = \frac{E}{1-\sigma^2}(u_{xx} + \sigma u_{yy}), \\ \sigma_{yy} = \frac{E}{1-\sigma^2}(u_{yy} + \sigma u_{xx}), \\ \sigma_{xy} = \frac{E}{1+\sigma}u_{xy}. \end{cases} \quad (23)$$

where σ_{xx} , σ_{yy} , σ_{xy} are the components of the stress tensor; u_{xx} , u_{yy} , u_{xy} are the components of the strain tensor; E is the Young's modulus and σ is the Poisson's ratio. For small deformations, the strain tensor is given by

$$u_{xx} = \frac{\partial u_x}{\partial x}, u_{xy} = \frac{1}{2}\left(\frac{\partial u_x}{\partial y} + \frac{\partial u_y}{\partial x}\right), u_{yy} = \frac{\partial u_y}{\partial y}. \quad (24)$$

where u_x, u_y are the components of the displacement vector. Substituting Eq. (23) and (24) into Eq. (22), we obtain the balance equations in terms of the displacement vector:

$$\begin{cases} \frac{1}{1-\sigma^2} \frac{\partial^2 u_x}{\partial x^2} + \frac{1}{2(1+\sigma)} \frac{\partial^2 u_x}{\partial y^2} + \frac{1}{2(1-\sigma)} \frac{\partial^2 u_y}{\partial x \partial y} = 0, \\ \frac{1}{1-\sigma^2} \frac{\partial^2 u_y}{\partial y^2} + \frac{1}{2(1+\sigma)} \frac{\partial^2 u_y}{\partial x^2} + \frac{1}{2(1-\sigma)} \frac{\partial^2 u_x}{\partial x \partial y} = 0. \end{cases} \quad (25)$$

Equations 25 can be written in the vector form

$$\nabla(\nabla \cdot \mathbf{u}(\mathbf{x})) - \frac{1}{2}(1-\sigma)\nabla \times (\nabla \times \mathbf{u}(\mathbf{x})) = 0, \quad (26)$$

where $\mathbf{u}(\mathbf{x})$ is the displacement vector at the point \mathbf{x} on the undeformed disk.

Upon the radial outward force f on the boundary, the disk is subject to radial stretching. We therefore search for the solution of rotational symmetry; i.e., the displacement vector $\mathbf{u}(\mathbf{x})$ is independent of the polar angle ϕ . Furthermore, the azimuthal component of the displacement vector is zero. In other words, the solution is in

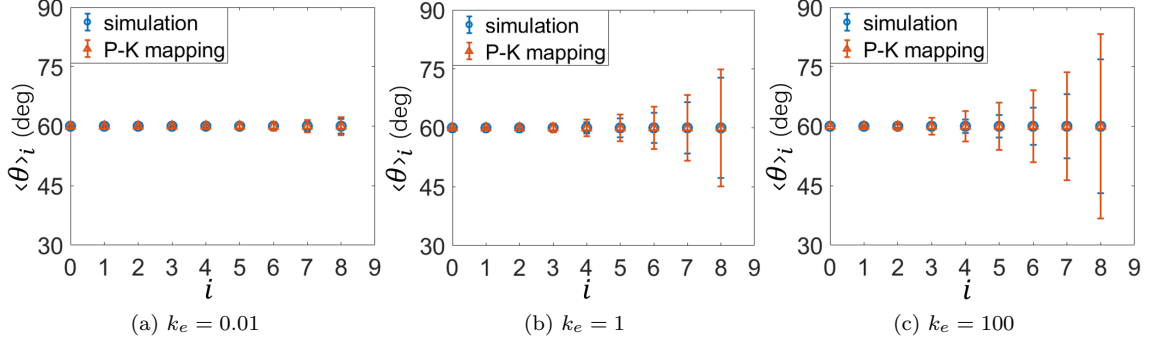


FIG. 9: Distributions of the average bond angle $\langle \theta \rangle_i$ in each layer i for both the lowest-energy configuration obtained by simulations (blue circle) and the configuration generated by the Poincaré-Klein mapping (orange triangle) at varying k_e . The averaging procedure in each layer is over all of the bond angles associated with each vertex along the layer. The magnitude of the standard deviation is indicated by the length of the error bars. The error bars associated with simulations are slightly shorter than those associated with the Poincaré-Klein mapping for large values of n in (b) and (c). $n = 9$. $k_b = 0.01$. The optimal values for the parameters λ and Γ in the Poincaré-Klein mapping, as well as the value for L , are listed here: (a) $\lambda = 0.010$, $\Gamma = 50.311$, $L = 0.002$. (b) $\lambda = 0.010$, $\Gamma = 51.541$, $L = 0.004$. (c) $\lambda = 0.004$, $\Gamma = 129.374$, $L = 0.011$.

the form of $\mathbf{u}(\mathbf{x}) = u_r(r)\hat{r}$. Here, we work in the polar coordinates (r, ϕ) . Equation (26) becomes

$$\nabla \cdot \mathbf{u} = \frac{1}{r} \frac{d(ru_r)}{dr} = \text{constant}. \quad (27)$$

We therefore have

$$u_r = C_1 r + \frac{C_2}{r}, \quad (28)$$

where the constants C_1 and C_2 are to be determined by the boundary condition. By applying the boundary conditions that the displacement is finite at $r = 0$ and $\sigma_{rr} = f$ at $r = R$, we finally obtain the expressions for the strain field:

$$u_{rr} = u_{\phi\phi} = \frac{1 - \sigma}{E} f, \quad u_{r\phi} = 0. \quad (29)$$

Equation (29) shows that the strain field created by the boundary radial force is homogeneous.

Appendix D: On the connection of the Poincaré disk and the Klein disk

In this appendix, we will show that under the Poincaré-Klein mapping the line element ds_p in the Poincaré disk is identical to the line element ds_k in the Klein disk.

Consider an arbitrary point (x_p, y_p) in the Poincaré disk. Under the Poincaré-Klein mapping [56]

$$f(z) = \frac{2z}{1 + |z|^2}, \quad |z| \leq 1, \quad (30)$$

it is mapped to (x_k, y_k) :

$$x_k = \frac{2x_p}{1 + x_p^2 + y_p^2}, \quad y_k = \frac{2y_p}{1 + x_p^2 + y_p^2}. \quad (31)$$

From Eqs.(31), we have

$$\begin{aligned} dx_k &= \frac{2(1 - x_p^2 + y_p^2)}{(1 + x_p^2 + y_p^2)^2} dx_p - \frac{4x_p y_p}{(1 + x_p^2 + y_p^2)^2} dy_p, \\ dy_k &= -\frac{4x_p y_p}{(1 + x_p^2 + y_p^2)^2} dx_p + \frac{2(1 + x_p^2 - y_p^2)}{(1 + x_p^2 + y_p^2)^2} dy_p. \end{aligned} \quad (32)$$

Therefore, the line element ds_k in the Klein disk is

$$ds_k^2 = \frac{dx_k^2 + dy_k^2}{1 - x_k^2 - y_k^2} + \frac{(x_k dx_k + y_k dy_k)^2}{(1 - x_k^2 - y_k^2)^2}. \quad (33)$$

By inserting Eqs. (31) and (32) into Eq. (33), we have

$$ds_k^2 = \frac{4(dx_p^2 + dy_p^2)}{(1 - x_p^2 - y_p^2)^2}. \quad (34)$$

The term in right hand side of Eq.(34) is recognized as ds_p^2 . Therefore, we have shown that $ds_k^2 = ds_p^2$ under the Poincaré-Klein mapping as defined in Eq.(30). This result is as expected, because both the Poincaré disk and the Klein disk represent the common hyperbolic plane.

V. ACKNOWLEDGEMENTS

This work was supported by the National Natural Science Foundation of China (Grants No. BC4190050).

- [1] Y. Levin, *Physica A* **352**, 43 (2005).
- [2] M. Leunissen, A. Van Blaaderen, A. Hollingsworth, M. Sullivan, and P. Chaikin, *Proc. Natl. Acad. Sci. U.S.A.* **104**, 2585 (2007).
- [3] D. A. Walker, B. Kowalczyk, M. Olvera de la Cruz, and B. A. Grzybowski, *Nanoscale* **3**, 1316 (2011).
- [4] M. A. Kostianen, P. Hiekkataipale, A. Laiho, V. Lemieux, J. Seitsonen, J. Ruokolainen, and P. Ceci, *Nat. Nanotechnol.* **8**, 52 (2013).
- [5] Y. Levin, *Rep. Prog. Phys.* **65**, 1577 (2002).
- [6] C. Holm, P. Kékicheff, and R. Podgornik, *Electrostatic Effects in Soft Matter and Biophysics* (Springer, Berlin, 2001).
- [7] P. P. Edwards and J. M. Thomas, *Angew. Chem. Int. Ed.* **46**, 5480 (2007).
- [8] I. Paci, I. Szleifer, and M. A. Ratner, *J. Am. Chem. Soc.* **129**, 3545 (2007).
- [9] K. L. Kohlstedt, F. J. Solis, G. Vernizzi, and M. Olvera de la Cruz, *Phys. Rev. Lett.* **99**, 030602 (2007).
- [10] G. Vernizzi and M. Olvera de la Cruz, *P. Natl. Acad. Sci. U.S.A.* **104**, 18382 (2007).
- [11] V. Jadhao, C. K. Thomas, and M. Olvera de la Cruz, *Proc. Natl. Acad. Sci. U.S.A.* **111**, 12673 (2014).
- [12] Z. Yao and M. Olvera de la Cruz, *Phys. Rev. Lett.* **116**, 148101 (2016).
- [13] C. Gao, S. Kewalramani, D. M. Valencia, H. Li, J. M. McCourt, M. Olvera de la Cruz, and M. J. Bedzyk, *Proc. Natl. Acad. Sci. U.S.A.* **116**, 22030 (2019).
- [14] G. Zaldivar, M. Conda-Sheridan, and M. Tagliazucchi, *J. Phys. Chem. B* **124**, 3221 (2020).
- [15] W. M. Gelbart, R. F. Bruinsma, P. A. Pincus, and V. A. Parsegian, *Phys. Today* **53**, 38 (2000).
- [16] A. Cherstvy, *Phys. Chem. Chem. Phys.* **13**, 9942 (2011).
- [17] A. Savelyev, C. K. Materese, and G. A. Papoian, *J. Am. Chem. Soc.* **133**, 19290 (2011).
- [18] G. S. Lee, Y.-J. Lee, and K. B. Yoon, *J. Am. Chem. Soc.* **123**, 9769 (2001).
- [19] D. A. Walker, K. P. Browne, B. Kowalczyk, and B. A. Grzybowski, *Angew. Chem. Int. Ed.* **49**, 6760 (2010).
- [20] S. K. Smoukov, K. J. Bishop, B. Kowalczyk, A. M. Kalsin, and B. A. Grzybowski, *J. Am. Chem. Soc.* **129**, 15623 (2007).
- [21] J. J. Thomson, *London Edinburgh Dublin Philos. Mag. J. Sci.* **7**, 237 (1904).
- [22] A. Bausch, M. Bowick, A. Cacciuto, A. Dinsmore, M. Hsu, D. Nelson, M. Nikolaidis, A. Travasset, and D. Weitz, *Science* **299**, 1716 (2003).
- [23] D. Mehta, J. Chen, D. Z. Chen, H. Kusumaatmaja, and D. J. Wales, *Phys. Rev. Lett.* **117**, 028301 (2016).
- [24] Z. Yao, *Phys. Rev. Lett.* **122**, 228002 (2019).
- [25] A. A. Berezin, *Nature* **315**, 104 (1985).
- [26] A. Mughal and M. Moore, *Phys. Rev. E* **76**, 011606 (2007).
- [27] Z. Yao and M. Olvera de la Cruz, *Phys. Rev. Lett.* **111**, 115503 (2013).
- [28] V. Soni, L. R. Gómez, and W. T. Irvine, *Phys. Rev. X* **8**, 011039 (2018).
- [29] M. J. Bowick and L. Giomi, *Adv. Phys.* **58**, 449 (2009).
- [30] D. R. Nelson, *Defects and Geometry in Condensed Matter Physics* (Cambridge University Press, Cambridge, 2002).
- [31] H. Hoffmann, C. Thunig, P. Schmiedel, and U. Munkert, *Langmuir* **10**, 3972 (1994).
- [32] J. Oberdisse, C. Couve, J. Appell, J. Berret, C. Ligoure, and G. Porte, *Langmuir* **12**, 1212 (1996).
- [33] B. Demé, M. Dubois, and T. Zemb, *Langmuir* **18**, 1005 (2002).
- [34] Z.-C. Ou-Yang and W. Helfrich, *Phys. Rev. A* **39**, 5280 (1989).
- [35] R. Capovilla, J. Guven, and J. Santiago, *Phys. Rev. E* **66**, 021607 (2002).
- [36] Y. Klein, E. Efrati, and E. Sharon, *Science* **315**, 1116 (2007).
- [37] Z. C. Tu, *Chin. Phys. B* **22**, 028701 (2013).
- [38] E. H. Yong, D. R. Nelson, and L. Mahadevan, *Phys. Rev. Lett.* **111**, 177801 (2013).
- [39] H. S. Seung and D. R. Nelson, *Phys. Rev. A* **38**, 1005 (1988).
- [40] Y. Schweitzer, T. Shemesh, and M. M. Kozlov, *Biophys. J.* **109**, 564 (2015).
- [41] Z.-C. Ou-Yang, J.-X. Liu, and Y.-Z. Xie, *Geometric Methods in the Elastic Theory of Membranes in Liquid Crystal Phases*, vol. 2 (World Scientific, Singapore, 1999).
- [42] M. Deserno, *Chem. Phys. Lipids* **185**, 11 (2015).
- [43] B. Duplantier, R. E. Goldstein, V. Romero-Rochn, and A. I. Pesci, *Phys. Rev. Lett.* **65**, 508 (1990).
- [44] T. Ambjörnsson, M. A. Lomholt, and P. L. Hansen, *Phys. Rev. E* **75**, 051916 (2007).
- [45] A. C. Rowat, P. L. Hansen, and J. H. Ipsen, *Europhys. Lett.* **67**, 144 (2004).
- [46] M. Winterhalter and W. Helfrich, *J. Phys. Chem.* **92**, 6865 (1988).
- [47] D. Andelman, in *Handbook of Biological Physics* (Elsevier, Amsterdam, 1995), vol. 1, pp. 603–642.
- [48] Y. Kantor and D. R. Nelson, *Phys. Rev. Lett.* **58**, 2774 (1987).
- [49] Y. Kantor and D. R. Nelson, *Phys. Rev. A Gen. Phys.* **36**, 4020 (1987).
- [50] R. Pathria and P. D. Beale, *Statistical Mechanics* (Academic Press, Cambridge, MA, 2011), 3rd ed.
- [51] P. Pierański, in *Phase Transitions in Soft Condensed Matter* (Springer, Berlin, 1989), pp. 45–48.
- [52] F. Rothen, P. Pierański, N. Rivier, and A. Joyet, *Eur. J. Phys.* **14**, 227 (1993).
- [53] K. W. Wojciechowski and J. Klos, *J. Phys. A: Math. Gen.* **29**, 3963 (1996).
- [54] R. M. Menezes, E. Sardella, L. R. Cabral, and C. C. de Souza Silva, *J. Phys.: Condens. Matter* **31**, 175402 (2019).
- [55] J. Chen and Z. Yao, *Soft Matter* **18**, 5323 (2022).
- [56] R. Benedetti and C. Petronio, *Lectures on Hyperbolic Geometry* (Springer, Berlin, 2012).
- [57] D. Krioukov, F. Papadopoulos, M. Kitsak, A. Vahdat, and M. Boguná, *Phys. Rev. E* **82**, 036106 (2010).
- [58] F. Battiston, G. Cencetti, I. Iacopini, V. Latora, M. Lucas, A. Patania, J.-G. Young, and G. Petri, *Phys. Rep.* **874**, 1 (2020).
- [59] R. Churchill and J. Brown, *Complex Variables and Applications* (McGraw Hill, New York, 2014).
- [60] L. D. Landau and E. M. Lifshitz, *Theory of Elasticity* (Butterworth-Heinemann, Oxford, 1986), 3rd ed.
- [61] P. W. S. Meital Reches and G. M. Whitesides, *Proc. Natl. Acad. Sci. U.S.A.* **106**(42), 17644 (2009).

- [62] R. Kumar, G. M. Coli, M. Dijkstra, and S. Sastry, *J. Chem. Phys.* **151**, 084109 (2019).
- [63] C. P. Kelleher, A. Wang, G. I. Guerrero-García, A. D. Hollingsworth, R. E. Guerra, B. J. Krishnatreya, D. G. Grier, V. N. Manoharan, and P. M. Chaikin, *Phys. Rev. E* **92**, 062306 (2015).
- [64] Z. Yao, *J. Phys.: Condens. Matter* **35**, 045101 (2023).
- [65] M. P. do Carmo and J. Flaherty Francis, *Riemannian Geometry*, vol. 6 of *Mathematics: Theory and Applications* (Springer, Berlin, 1992).